Experimental Investigation of Interfacial Mass Transfer Mechanisms for a Confined High-Reynolds-Number Bubble Rising in a Thin Gap

Matthieu Roudet
Laboratoire de Génie Chimique, Université de Toulouse, CNRS-INPT-UPS, Toulouse, France

Institut de Mécanique des Fluides de Toulouse (IMFT), Université de Toulouse, CNRS-INPT-UPS, Toulouse, France

FERMAT, Université de Toulouse, CNRS, INPT, INSA, UPS, Toulouse, France

Anne-Marie Billet
Laboratoire de Génie Chimique, Université de Toulouse, CNRS-INPT-UPS, Toulouse, France

FERMAT, Université de Toulouse, CNRS, INPT, INSA, UPS, Toulouse, France

Sébastien Cazin, Frédéric Risso, and Véronique Roig
Institut de Mécanique des Fluides de Toulouse (IMFT), Université de Toulouse, CNRS-INPT-UPS, Toulouse, France

FERMAT, Université de Toulouse, CNRS, INPT, INSA, UPS, Toulouse, France

DOI 10.1002/aic.15562

Interfacial mass transfer is known to be enhanced for confined bubbles due to the efficiency of the transfer in the thin liquid films between them and the wall. In the present experimental investigation, the mechanisms of gas–liquid mass transfer are studied for isolated bubbles rising at high Reynolds number in a thin gap. A planar laser induced fluorescence (PLIF) technique is applied with a dye the fluorescence of which is quenched by dissolved oxygen. The aim is to measure the interfacial mass fluxes for pure oxygen bubbles of various shapes and paths rising in water at rest. In the wakes of the bubbles, patterns due to the presence of dissolved oxygen are observed on PLIF images. They reveal the contrasted contributions to mass transfer of two different regions of the interface. The flow around a bubble consists of both two thin liquid films between the bubble and the walls of the cell and an external high-Reynolds-number in-plane flow surrounding the bubble. Mass transfer mechanisms associated to both regions are discussed. Measurement of the concentration of dissolved oxygen is a difficult task due to the nonlinear relation between the fluorescence intensity and the concentration in the gap. It is however possible to accurately measure the global mass flux transferred through the bubble interface. It is determined from the fluorescence intensity recorded in the wakes when the oxygen distribution has been made homogeneous through the gap by diffusion. Assuming a reasonable distribution of oxygen concentration through the gap at short time also allows a measurement of the mass fluxes due to the liquid films. A discussion of the results points out the specific physics of mass transfer for bubbles confined between two plates as compared to bubbles free to move in unconfined flows.

Keywords: confined bubble, interfacial mass transfer, Planar Laser Induced Fluorescence with Inhibition (PLIFI) technique

Introduction

During the three last decades, small scale structured reactors and monolith reactors have been considered as a viable alternative to the conventional three-phase reactors such as trickle beds, slurry bubble columns, or large scale batch reactors. This new kind of reactor are often seen as very promising[1–3] especially in terms of space or time yield and in terms of chemical selectivity. A review from Jensen (2001) reports the main general advantages expected from micro- or milli-structured reactors.[4] Among them, their good ability to reduce heat and mass transfer resistance is crucial for fast and highly exothermic reactions. The good performance observed for fast reactions in confined gas–liquid reactors is attributed to the fact that these reactions are limited by mass transfer, and that high mass transfer rates between phases take place in these

Table 1. Physical Properties of the Mixture

Water (% vol/vol)	Ethanol (% vol/vol)	C_R (mg/L)	ρ (kg/m^3)	μ (Pa.s)	σ (mN/m)	$D \times 10^9$ (m^2/s)	$C_s(mg/L)$
80	20	25	970 [25] or 965 [23]	0.0010 [25]· [23]	38.56 [21] or 38.9 [23]	1.9 [25] or 2.04 [24]	45 [26]

C_R is dye concentration. The capillary length $l_c=\sqrt{\sigma/\rho g}$ is about 2 mm, with g the acceleration of gravity.

confined flows. Kreutzer et al. (2006) compared mass transfer efficiency between gas and liquid phases in various types of reactors and established that the global volumetric gas–liquid mass transfer coefficient k_La is 2–7 times greater in monolith reactors or capillary channels than in large turbulent contactors.[5] It is often believed that mass transfer efficiency is mainly due to bubble confinement, leading to an efficient transfer of gas reactant toward the thin liquid films between bubbles and walls.[1,6] Two opposite cases can nevertheless be clearly distinguished, depending on the saturation rate in the liquid film. For Taylor bubbles in capillary tubes, it has been shown that this saturation depends on the value of the contact time between bubbles and films, t_{film},[7] or on the Fourier number of the liquid film $Fo=D.t_{film}/h^2$ (where D is the mass diffusivity and h the width of the film).[8] When Fo is small (lower than 0.1 typically), or when a catalytic reaction consumes dissolved gas at the wall, the liquid film is far from saturation in dissolved gas; for long contact times in absence of catalytic reaction, the film may be saturated. When the liquid film is not saturated, the contribution of the film to the gas–liquid mass transfer is dominant as shown in the experimental results obtained by Vandu et al. (2005) for non-reactive absorption of oxygen in water with short bubbles.[7] In contrast, when the liquid films are close to saturation in dissolved gas, the contribution of films is ineffective and mass transfer takes place between the bubble caps and the liquid slugs. Models for such mass transfer around Taylor bubbles have been proposed.[7–12] To improve the generality of the models, it would be interesting to find a way to sort out experimentally the simultaneous contributions of mass transfer from the liquid films and from the bubble caps, in absence of any chemical reaction and with non-saturated films, to compare their relative importance and to relate them to the main physical parameters of the problem: bubble and slug sizes, film thickness and phases velocities. This requires experimental investigations of the local concentration field in the vicinity of the bubbles, as recently achieved with colorimetric methods.[13]

In this work we explore mass transfer at the gas–liquid interface of an isolated bubble rising at high Reynolds number in a liquid at rest confined in a planar thin gap. The flow is confined as in monoliths with Taylor bubbles, but the configuration and the dynamics of the thin liquid films between the bubble and the walls are different. The dynamics of such bubbles have been already explored for a large range of Archimedes number.[14,15] In this inertial regime, bubble motion is strongly coupled to the wake dynamics and several regimes of oscillating shapes and/or trajectories are observed depending on the Archimedes number. The motions induced in the liquid phase are in-plane motions strongly dampened by shear stress at walls. While the Reynolds number of the in-plane flow around the bubble is large, the fluid is almost at rest in the liquid films between the bubble and the walls. Whereas these liquid films do not influence the bubble dynamics, they play a significant role in mass transfer. Homogeneous bubbly flows confined in a thin gap also prove to promote intense agitation and mixing in the liquid phase.[16–18] The planar confinement generates the presence of thin liquid films between the bubbles and the walls while the in-plane motions of the bubbles and the liquid have both two degrees of freedom. The mixing of a passive scalar of low molecular diffusivity by the agitation generated by the rising bubbles is therefore efficient. It is however not compatible with a Fickian diffusion process as the transport of the scalar is performed by its chaotic advection in the wakes of the bubbles.[17,19]

In the present work, we want to examine if the noticeable increase of mass transfer observed in monolith bubbly reactors is still preserved in a planar bubbly flow that can be used in photochemical reactors, for example. The article is organized as follows. Section "Experimental Methods" describes the experimental technique. Section "Mechanisms for Mass Transfer" presents the mechanisms involved in mass transfer while section "Measurement of Mass Fluxes and Discussion" is devoted to the measurement of the mass fluxes and section "Concluding Remarks" summarizes the main findings.

Experimental Methods

Description of the set-up and experimental conditions

The experimental cell is made of two vertical glass plates with dimensions 400 × 800 mm separated by a thin gap of width $w=$ 1 mm, which is smaller than the capillary length of the fluid[14] ($l_c \approx 2$ *mm* as detailed in Table 1). It is filled with a liquid at rest. Isolated bubbles of pure oxygen are injected at the bottom through a capillary-tube and rise in the plane of the cell. The liquid aqueous mixture is selected to measure oxygen interfacial mass transfer using planar laser induced fluorescence (PLIF) technique. It consists of a mixture of distilled water, ethanol, and dissolved ruthenium complex. The physical properties of this mixture are close to those of the corresponding water–ethanol mixtures as discussed hereafter. The top of the cell is open so that the bubble can disengage easily. Before any mass transfer measurement, the liquid in the cell is totally de-oxygenated by bubbling nitrogen for a long time before injection of a bubble of pure oxygen. The bubble size is larger than the gap. As the bubble is strongly flattened between the walls, it moves in the (x, y) plane (Figure 1a) and the motions it induces in the liquid are, except in its very near vicinity, in-plane motions. Due to wetting physical conditions, thin liquid films always exist between the bubble and the walls. The size of the bubble is defined as the equivalent diameter d of its in-plane projected area $S=\pi d^2/4$. The oxygen inlet system consists of a small valve that is operated by hands. The size of each bubble is accurately measured from recorded images. The bubble diameters d lay between 5.1 and 32 mm so that the ratio w/d is lower than 0.2. For mass transfer analysis it is important to evaluate both the area of a liquid film S_f and the area of the peripheral interface in contact with the in-plane flow S_p (Figure 1a). For thin liquid films of width h negligeable as compared to w, the measurements of the projected area S and of the perimeter P of this projected surface

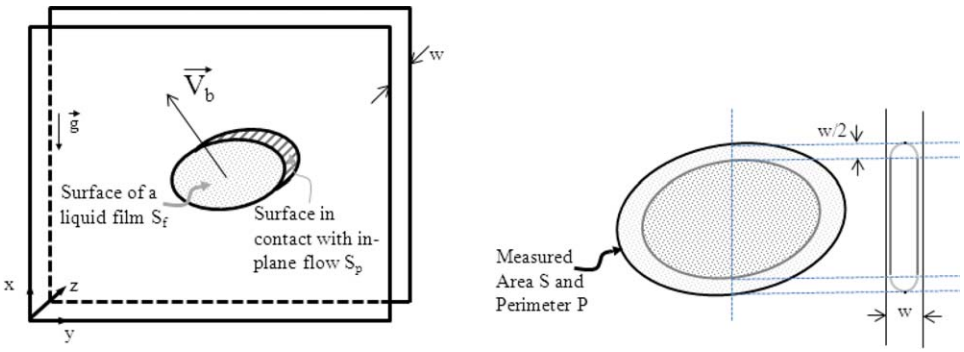

Figure 1. (a) Schematic representation of a bubble flattened between two plates. (b) Estimation of the surface areas of the liquid films and of the bubble in contact with the in-plane flow.

[Color figure can be viewed at wileyonlinelibrary.com]

provide the estimations of S_f and of S_p as $S_f = S - \frac{w}{2} P$ and $S_p = \pi \frac{w}{2} P$ (Figure 1b).

To apply the PLIF technique to mass transfer measurement, a specific fluorescent dye, named tris-(4,7 diphenyl-1,10-phenantroline) Ruthenium (II) bis-perchlorate (CAS: 75213-31-9), is dissolved into the water used to fill the cell.[20] This dye is purchased in small flasks of 500 mg of powder. A moderate amount of ethanol is added to the water to help the dissolution of the dye and to obtain a homogeneous solution. To reach a convenient fluorescence yield, the concentration of the dye has been chosen to 25 mg/L. The concentration of ethanol in the dye solution is 20% vol. It has been verified that the evaporation of ethanol in the cell during the experiments is negligible. The average temperature remained close to 20°C during the experiments.

For this solution consisting of a mixture of distilled water, ethanol, and dissolved ruthenium complex, the values of the liquid density ρ, dynamic viscosity μ and surface tension σ remain close to the values of the corresponding water–ethanol mixtures. The properties of the used solution, calculated on the basis of published experimental data[21,22] are given in Table 1. The values of ρ, σ, and μ have also been directly measured for the used mixture by Jimenez et al.[23] and proved to be in agreement with the calculated properties. We can thus consider that the parameters given by Vazquez et al.[21] and Pecar et al.[22] are relevant for our mixture.

Concerning mass transfer, bubbles contain pure oxygen and rise in a de-oxygenated dye solution. The diffusivity D of oxygen in water–ethanol solutions at 20°C can be estimated from the relation given by Wilke and Chang.[24] Its value is reported in Table 1. A direct measurement of the diffusivity was also performed by Jimenez et al.[25] for the used mixture. The prediction of D fits the measured value and the properties of the mixture are thus precisely known from the measurements of Jimenez et al.[23,25] The equilibrium concentration of dissolved oxygen at bubble interface C_s is expected to be very close to the equilibrium concentration of dissolved oxygen in corresponding water–ethanol mixture. At 20°C and 1 atm, the value of C_s can be obtained from Reid et al.[26] and is given in Table 1. We have experimentally verified with an OX-10 oxygen probe and an oxymeter (Unisense technology) that C_s is similar to the equilibrium concentration of dissolved oxygen in water–ethanol mixture.

The non-dimensional numbers that characterize the problem are the confinement ratio w/d, the Archimedes number $Ar = \frac{\rho\sqrt{gd}d}{\mu}$, the Bond number $\frac{\rho g d^2}{\sigma}$, and the Schmidt number $Sc = \frac{\mu}{\rho D}$ (where g is the acceleration of gravity). Sc is large, around 500, Ar varies in the approximate range 200–18,000, Bo in the range 1–200 and w/d is always lower than 0.2. In such conditions, the dynamics are those of an isolated strongly confined bubble as studied in pure water by Roig et al.[14] for similar ranges of parameters. The fluid dynamics and mass transfer rates are expected to be different in the liquid films and in the in-plane flow surrounding the free periphery of the bubble. Indeed, the Reynolds number of the bubble ($Re = \frac{\rho V_b d}{\mu}$) and that of the film ($Re = \frac{\rho V_b h_f}{\mu}$) are very different (with V_b the velocity of the bubble and h_f the film thickness) since $h_f \ll d$. The films do not participate significantly to the bubble dynamics[14] but we will see in this study how they contribute to mass transfer. In the considered range of non-dimensional parameters, bubbles with stable or periodic trajectories, with constant or oscillating shapes, have been observed depending on the wake dynamics.[14] The smallest confined bubbles have nearly cylindrical in-plane projected shapes and rise steadily as their wake is stable. Then, when the bubbles increase in size, they adopt an elliptical in-plane shape and start to oscillate due to the destabilization of their wake. Further increase of the volume leads to simultaneous shape and path in-plane oscillations. For large bubbles ($Ar \gtrsim 10^4$) the shape is circular cap and the path is stationary as their wake has recovered a stable state. The confinement imposes a rapid decay of the flow induced in the liquid phase by each bubble passage, because of the shear stress exerted at the walls. The time for the flow to vanish scales with the viscous time w^2/v (where v is the kinematic viscosity),[14] and 1 s after the bubble passage the liquid is at rest. Due to the added ethanol, the bubble dynamics changes for a given bubble size d as compared to its dynamics in pure water. The scaling law giving the mean velocity of the bubble as a function of the equivalent radius $r_{eq} = (3/16 d^2 w)^{1/3}$ of the sphere having the same volume as the bubble given in Filella et al.[15] is conserved but with a different prefactor compared to pure water. While it writes $V_b \approx \sqrt{g r_{eq}}$ in pure water, it is best fitted by $V_b = k\sqrt{g r_{eq}}$ with $k = 0.715$ in the present mixture. This is due to the change of surface tension, that causes a slight changes to the shape for a given volume of the bubble. It remains that the same successive regimes of path and shape oscillations are observed in the water–ethanol mixtures as in pure water.

PLIF technique with quenching

PLIF is a measurement technique used to visualize a fluorescent dye in a planar section of a flow. It may be used to study mixing of an injected fluorescent dye (see the review of Crimaldi[27] for mixing in aqueous flows) or to analyse the interfacial transfer of a molecular component. The PLIF

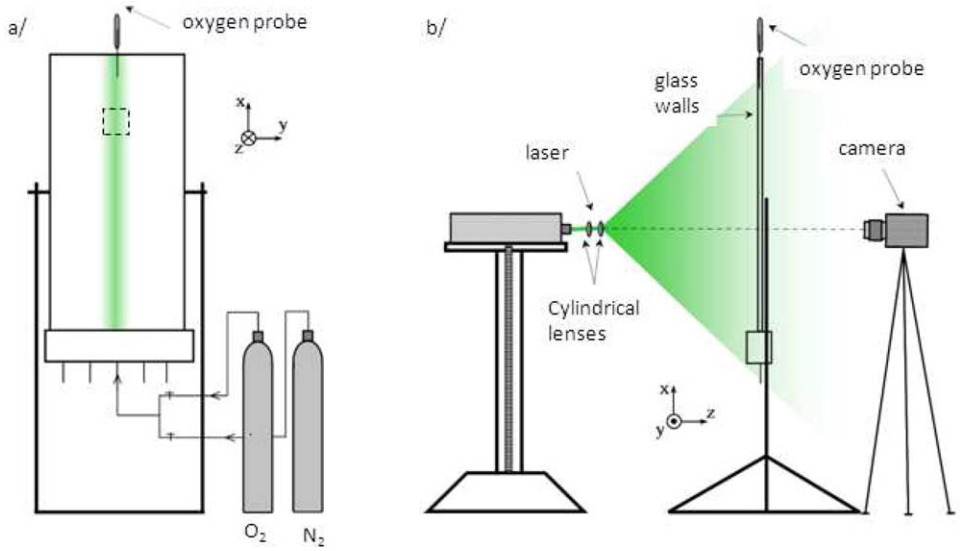

Figure 2. Experimental set-up

[Color figure can be viewed at wileyonlinelibrary.com]

technique consists in exciting a fluorescent dye with a light at a wavelength that the dye can absorb. Fluorescence being emitted by the dye at a higher wavelength, it is possible to separate both excitation and fluoresced lights. For mixing studies, the fluoresced light intensity is directly related to the fluorescent dye concentration. For interfacial mass transfer measurements in gas–liquid applications, PLIF techniques with quenching, denamed PLIFI for PLIF techniques with Inhibition, have been developped.[20,23,28–31] In the present case, the concentration of fluorescent dye is uniform in the liquid phase. The dye is chosen because its intensity of fluorescence is inhibited by the molecule which is transferred at the interface. This inhibition is proportional to the molecule concentration in the liquid phase. To study oxygen transfer in water two dyes have commonly been used as mentioned in literature. The first dye is pyrene butyric acid.[29,32] Its fluorescence is excited and has to be observed in UV-light and therefore requires specific fused silica windows. For this study the complex of ruthenium used by Dani et al.[20] that can be excited by a laser operating at 532 nm was chosen.

Specific PLIF Measuring System. For PLIF experiments, a specific experimental system has been used (Figure 2). A Quantel multipulse Nd:YAG laser (532 nm, 2 × 200 mJ) provides the excitation light. The laser beam belongs to an horizontal plane, but it is tilted of 30° with regard to the plates to avoid direct light to the camera and direct reflection of the light back to the laser cavity. Cylindrical lenses make the beam divergent to obtain a large interrogation zone in the cell ($566 < x < 640$ mm; $241 < y < 300$ mm). In this interrogation zone the whole layer of liquid is lighted. The interrogation zone is filmed by a CCD camera (sensicam PCO 12-bits, 1280 × 1024 pixels) settled normal to the plates, in front of the laser and equipped with an objective of 85 mm focal length and a high-pass filter to separate the excitation light from the fluoresced one. The integration time of the camera is set to 100μ s. The measurement resolution is 77.3 μm/pixel. The sampling frequency, imposed by the synchronization between the laser pulse and the camera, is 10 Hz. The number of successive frames recorded in one experiment is around 200. Each sequence may be recorded at a short time or at a long time (typically 200–300 s) after the bubble passage depending on the measurement to be performed, as explained hereafter.

Concentration of dissolved oxygen in the bulk is also checked using a Unisense system equipped with an OX-10 oxygen probe settled at the top of the cell. Prior to any record, nitrogen bubbles are introduced into the test cell to purge the oxygen from the solution. An initially low dissolved oxygen concentration of 0.1 mg/L (according to the precision of the oxymeter) is achieved after 10 min of bubbling. Then, mass transfer experiments are started and pictures of bubbles of pure oxygen rising in the de-oxygenated solution and of their wakes are recorded.

Relation between Fluorescence and Concentration of Dissolved Oxygen. The absorption and emission spectra of the present fluorescent dye have been measured and reported in Figure 3. The extend of the absorption spectrum shows that the dye has to be excited by a light with a wavelength lying between 450 and 540 nm. When excited, the dye emits fluorescence at wavelengths around 650 nm (see emission spectrum on Figure 3). The absorption and emission spectra of the dye do not overlap each other. This allows the recorded fluorescence signal to be easily separated from both the scattered laser light and the ambient light by use of the high-pass optical filter mounted in front of the camera. The wavelength of the incident laser light is 532 nm. This excitation source is thus not optimal for this dye that would be best excited at 450 nm. However, when the laser is used at its maximum power (200 mJ), the excitation light is sufficient to ensure a good contrast between fluorescent areas and non-fluorescent areas (approximately 700 grey levels in recorded images). This dye has also the property to be quenched when dissolved dioxygen is present in the solution. The attenuation of the intensity of the emitted fluorescent light is illustrated in Figure 3. This property is used to perform measurements of dissolved dioxygen concentrations by PLIFI.

The fluorescence intensity from an elementary volume of liquid in the cell is denoted F in the presence of dioxygen and F_0 in its absence. Both intensities F and F_0 are related to the oxygen concentration, C, by the Stern-Vollmer equation[20]:

$$\frac{F}{F_0} = \frac{1}{1 + K_{SV} C} \tag{1}$$

where K_{SV} is the Stern-Vollmer constant. This constant for the Ruthenium complex used as a dye can be obtained from a

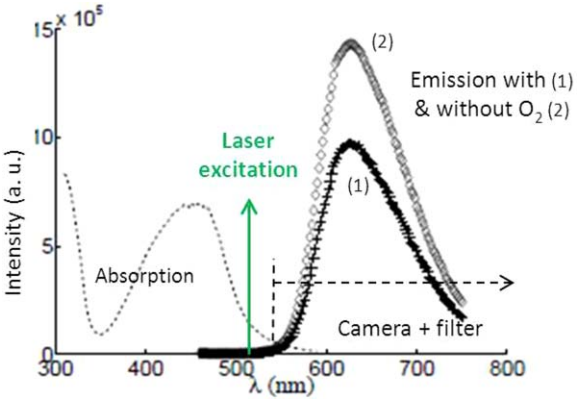

Figure 3. Spectra of absorption and of emission of the dye.

The emission spectra have been measured with an excitation at 450 nm. The emission is different with (1) and without (2) oxygen in the liquid. The laser wavelength and the bandwidth of light collected by the camera are also shown. [Color figure can be viewed at wileyonlinelibrary.com]

calibration procedure. Equation 1 is used to determine the dye concentration from measurements of F and F_0.

It is important to notice that, since the Stern-Vollmer relation is nonlinear, the interpretation of the fluorescence signal recorded by the camera at a measuring location (x, y) is not straightforward when the fluorescence intensity (that is when the oxygen concentration) is not uniform in between the plates of the cell.

If the dissolved oxygen concentration is not uniform across the liquid gap associated to direction z, the measured fluorescence intensity $F(x,y,t)$ results from the contribution of each elementary volume of fluid in the z-direction and can be expressed as:

$$\frac{F(x,y,t)}{F_0(x,y,t)} = 1/w \int_0^w \frac{1}{1+K_{SV}C(x,y,z,t)}dz \qquad (2)$$

It is thus not possible to deduce directly the planar distribution of concentration averaged over the gap $\bar{C}(x,y,t)=1/w\int_0^w C(x, y, z, t)dz$ from the planar distribution of fluorescence $F(x,y,t)$.

Note that, in relation (2), we have assumed that absorption of the laser excitation light and of the fluoresced light throughout the cell along z is negligible. In fact, the absorption coefficient $\sigma_W(\lambda_1)$ of the present aqueous solution is equal to 0.5 m^{-1} at the wavelength $\lambda_1 = 530$ nm (near that of the laser) and equal to $\sigma_W(\lambda_2)$=0.4 m^{-1} at $\lambda_2 = 600$ nm (within the emission spectrum of the dye). By applying the Beer-Lambert law, crossing the cell, the light is attenuated of a ratio $I_{laser}(z=w)/I_{laser}(z=0) \approx \exp(-\sigma_W(\lambda_1).w)$. The relative variation of the excitation light intensity in the direction normal to the plates is thus less than 0.05%. In the same way, the attenuation of the fluoresced light within the cell is negligible: $F(z=w)/F(z=0) \approx \exp(-\sigma_W(\lambda_2).w) \approx 0.04\%$. With or without quencher, absorption throughout the cell is negligible. The cell can therefore be considered as an optically thin system.

Image Processing and Calibration. The camera sensor records grey levels resulting from different light contributions as well as the camera noise I_{0cam}, which can be measured when the camera is shut. The intensity measured by the camera in the absence of dye and of quencher is named I_{exc}. The intensity $I_{exc}-I_{0cam}$ is the residual laser light that is not eliminated despite the high-pass filter. The intensity recorded by the camera in the presence of dye and with no quencher, named I_0, combines the residual laser light and fluoresced light. The fluorescence intensity F_0 is thus measured by applying the relation: $F_0=I_0-I_{exc}$. Finally the intensity recorded by the camera in the presence of dye and of oxygen, denoted I, combines the residual laser light and the fluoresced light modified by quenching. The fluorescence intensity F is then obtained by $F=I-I_{exc}$.

When no quencher is present, the fluorescence intensity F_0 is related to the total laser excitation intensity I_{laser} and to the concentration of dye (see Crimaldi[27] for general fluorescence laws). When the excitation intensity is too large, saturation effects may lead to a nonlinear relation. It has been verified in the present work that the relation between F_0 and I_{laser} is linear for the chosen experimental conditions. For that purpose the laser power was varied and, using a maximal optical aperture, $I_{exc}-I_{0cam}$ was measured in the absence of the dye. Then the intensity F_0 (with dye and in the absence of oxygen) was also measured at the same laser intensities. The test proved satisfactory since a linear relation has been found between $<F_0>$ and $<I_{exc}-I_{0cam}>$, the intensities averaged over the observation window.

The Stern-Vollmer constant K_{SV} is determined by a calibration performed at constant laser power: for various uniform concentrations of dissolved oxygen in the cell obtained by bubbling oxygen for various time durations, the concentration is measured with the Unisense oxymeter and the associated fluorescence intensity is recorded simultaneously. The linear relation between $\frac{F_0}{F}$ and C has been checked to be valid for the intensities $\langle F \rangle$ and $\langle F_0 \rangle$ averaged over the observation window. The constant K_{SV} has been found equal to 0.48 L/mg. This value is consistent with previous work.[20] Hence, in conditions of uniform distribution across the gap, the dissolved oxygen concentration C can be determined by measuring the local intensity of the emitted fluorescence with and without oxygen.

Spatial and temporal fluctuations of the incident laser light induced by the use of the spherical lens cannot be neglected. Raw images of the interrogation area in the absence of oxygen for a homogeneous mixture show that the fluorescence light is neither uniform over the interrogation area nor constant with time at any (x, y) location (Figure 4). It has been experimentally proved however that the total fluorescence energy E, calculated from a spatial integration of the intensity, is conserved with time. These fluctuations are always lower than 2.5% of the time-averaged value of E. This states that the total intensity of the laser pulse is reproducible in time.

It is nevertheless possible to overcome the important problem of spatial and temporal fluctuations of the light by use of time-averaged images of the cell before bubble injection and time-averaged images of the immobilized wake of oxygen after the passage of a bubble.

Time-averaged images of the interrogation zone converge toward constant levels of fluorescence intensity as soon as more than 15 consecutive frames are considered. The uncertainties due to time and spatial fluctuations disappear in these images as shown in Figures 5a, b where two averaged profiles obtained from different series of images superpose. These time-averaged images then reveal the mean nonuniform intensity due to the spatial distribution of light of the laser source.

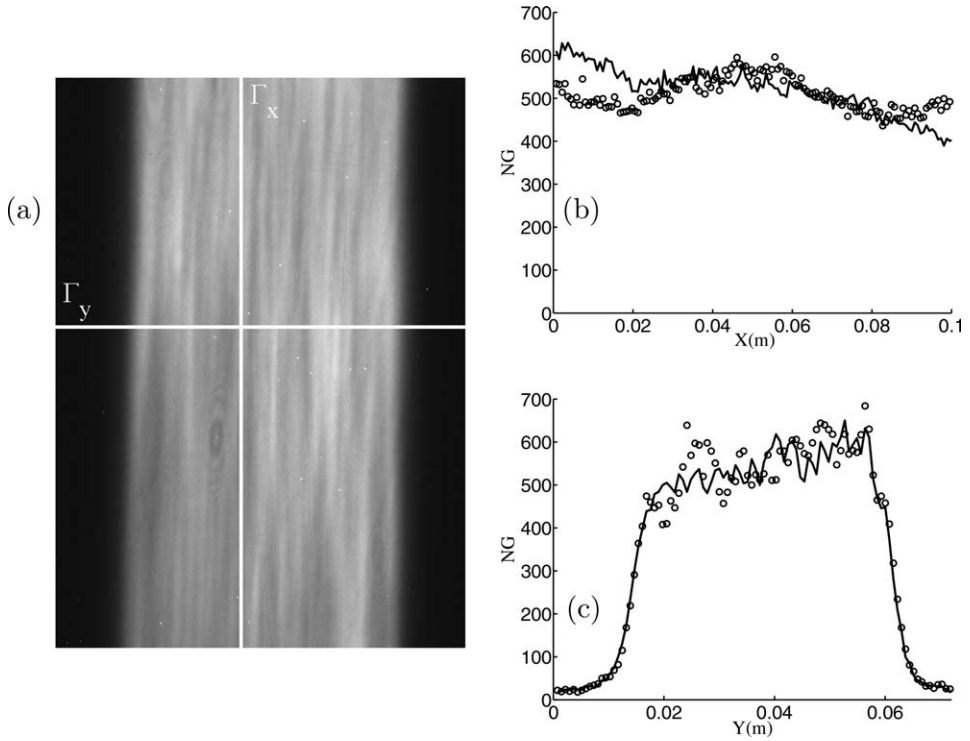

Figure 4. (a) Instantaneous image recorded by the camera showing fluctuations of fluorescence for a homogeneous mixture in the liquid with no quencher. Γ_x and Γ_y are lines along which the grey levels are displayed. (b, c) Instantaneous grey level profiles along Γ_x and Γ_y lines. Continuous line and circles represent the spatial distributions at two times separated by 0.1 s.

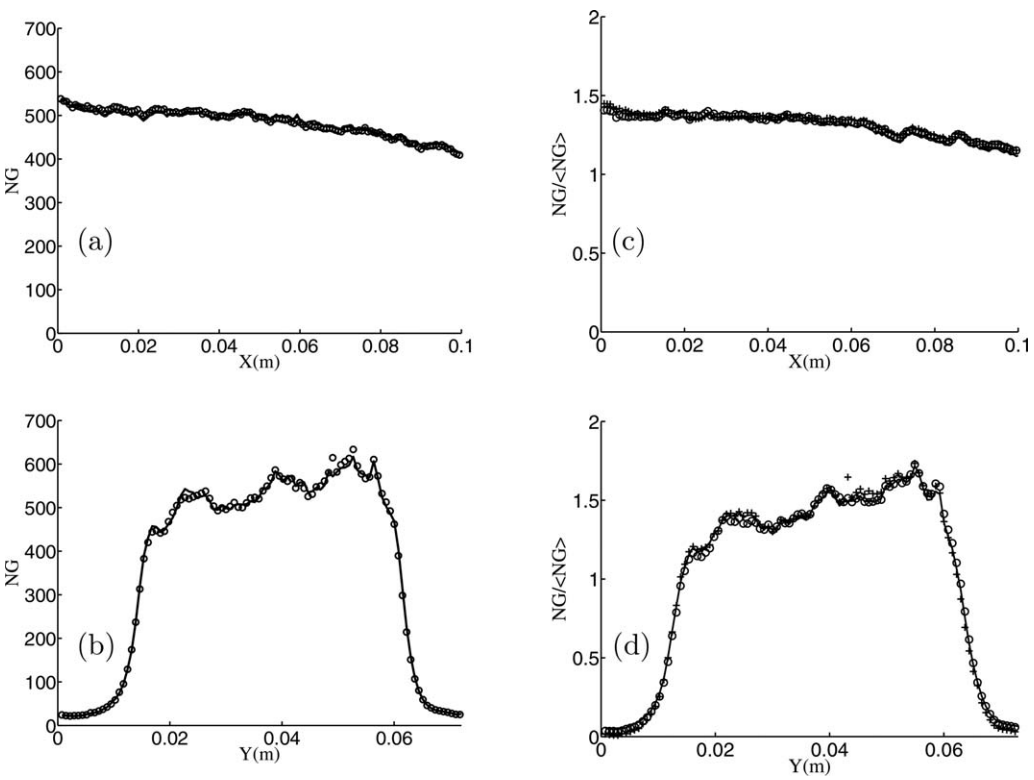

Figure 5. (a, b) Time-averaged grey level profiles along Γ_x and Γ_y lines. Continuous line and circles represent two spatial distributions averaged over two nonoverlapping series of 15 images. Their superposition indicates that time-averaging eliminates spurious fluctuations. (c, d) Time-averaged grey levels profiles normalized by their space averaged value (averaged over the observation window) for several oxygen concentrations ((c) along Γ_x line and d/along Γ_y lines). $C = 0$ mg/L: continuous line, $C = 2.41$ mg/L: + and $C = 8.5$ mg/L: *o*. The superposition shows that calibration obtained from spatially averaged images is also valid at any pixel position.

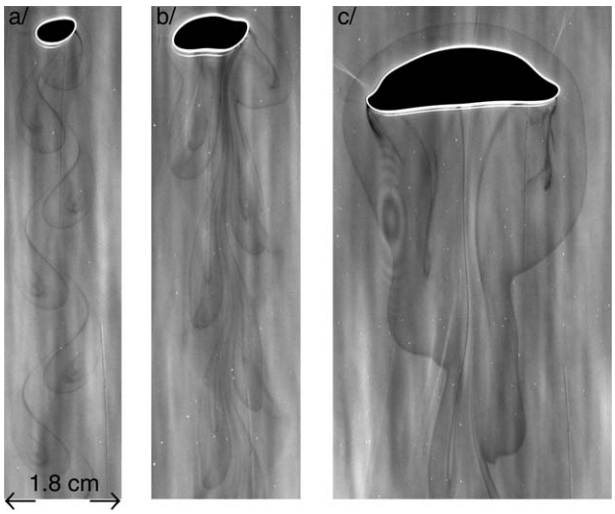

Figure 6. Instantaneous PLIF images for *Ar*=1,200 2,380, and 6,340.

Bubbles are seen in black with a white contour. Oxygen dissolved in the liquid field is revealed in the darker regions since it quenches dye fluorescence.

The non-uniform lighting of the laser in the plane (x, y) is not a problem when applying the Stern-Volmer equation as it involves the ratio of the local values of F and F_0 which both include the nonuniformity effect. In Figures 5c, d the ratio between the local values of F and the value averaged over the observation window $\langle F \rangle$ are plotted for several situations of homogeneous oxygen concentration. The ratio is independent of the considered oxygen concentration. This proves that the calibration curve may be applied for any pixel as well as for spatially averaged images.

For a bubble of pure oxygen rising in a de-oxygenated solution in the cell, the raw instantaneous PLIF images show patterns of quenched fluorescence intensity in bubble wakes, proving the presence of dissolved oxygen (Figure 6). On these pictures, the whole lighted area is submitted to spatial and time fluctuations of excitation intensity. It is thus impossible to use these instantaneous images to measure accurately the oxygen concentration distribution near bubble interfaces or in bubble wake. However, as the perturbation of velocity induced in the liquid phase by the bubble passage vanishes rapidly due to the shear stress exerted at the walls, it is possible to observe the oxygen deposit in bubble wake once immobilized. Calculating time averaged image in the liquid at rest allows to eliminate the spatial and temporal fluctuations of the laser. As mentioned before, the time necessary for the velocity perturbation to be dampened is given by the characteristic viscous time w^2/v equal to 1 s. We thus wait for 1–2 s after bubble departure to capture 25 images of the wake and average them to define the image to be processed $I(x, y)$. During the time of record ($\delta t \approx 2.5$ s), oxygen migrates by molecular diffusion by less than $(D\delta t)^{1/2} \approx 70$ μm, which is lower than the pixel size. As a consequence, for such short time series, time averaging does not alter the measurement of the spatial in-plane distribution of oxygen. A series of 25 images is also recorded before bubble injection in the same experimental conditions, with totally de-oxygenated solution. This series of images is time-averaged too and the result provides the reference image $I_0(x, y)$. During measurements of oxygen transfer we used a low optical aperture so that the averaged image associated to I_{exc} in the absence of dye and oxygen is nearly equal to the average associated to I_{0cam}. Considering averaged images only, for situations where the oxygen concentration C is uniformly distributed across the gap, the dissolved oxygen concentration is calculated by applying relation (1) with $F_0 = I_0 - I_{0cam}$ and $F = I - I_{0cam}$. Note that, at short times after the bubble passage, oxygen distribution is not uniform across the gap, but a model for this distribution has been developed to use relation (2) and to determine the average oxygen concentration. This model is discussed later on. As will be shown in the following, the described image processing results in a good signal-to-noise ratio (larger than 20).

Mechanisms for Mass Transfer

The spatial distribution of fluorescence just one second after the passage of isolated bubbles is reported in Figure 7 for various Archimedes numbers in the range from 210 to 18,000. For clarity purpose, we have reported $(1 - R_{fluo})$ instead of

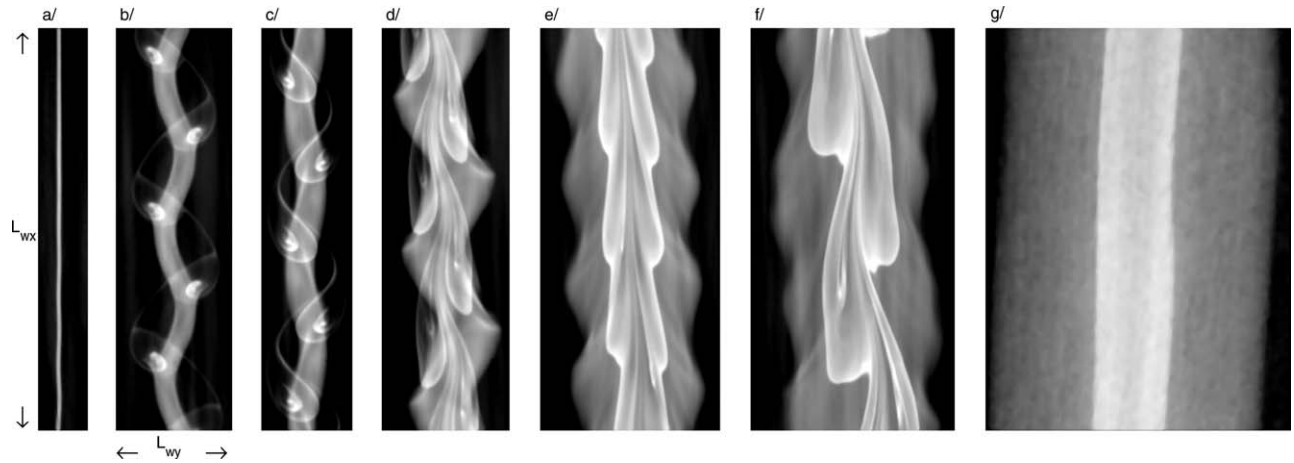

Figure 7. Averaged PLIF images in term of $(1-R_{fluo})$ in the wakes of bubbles of various Archimedes numbers: *Ar*=210; 1,016; 1,200; 2,380; 5,016; 6,340; and 18,000, respectively, for cases (a–g).

Gravity vector is oriented from top to bottom. The images are recorded from 1.6 to 2.5 s after bubble passage. For better representation, the PLIF signal has been inverted so that white color means oxygen presence. For this visualization, length scale in vertical direction is the same for all runs (L_{wx} = 6.9 cm); length scale in horizontal direction, L_{wy}, varies from case to case: L_{wx}/L_{wy} = 8.13, 3.47; 4.43, 3.15, 2.24, 1.97, 1.32 for the successive *Ar*.

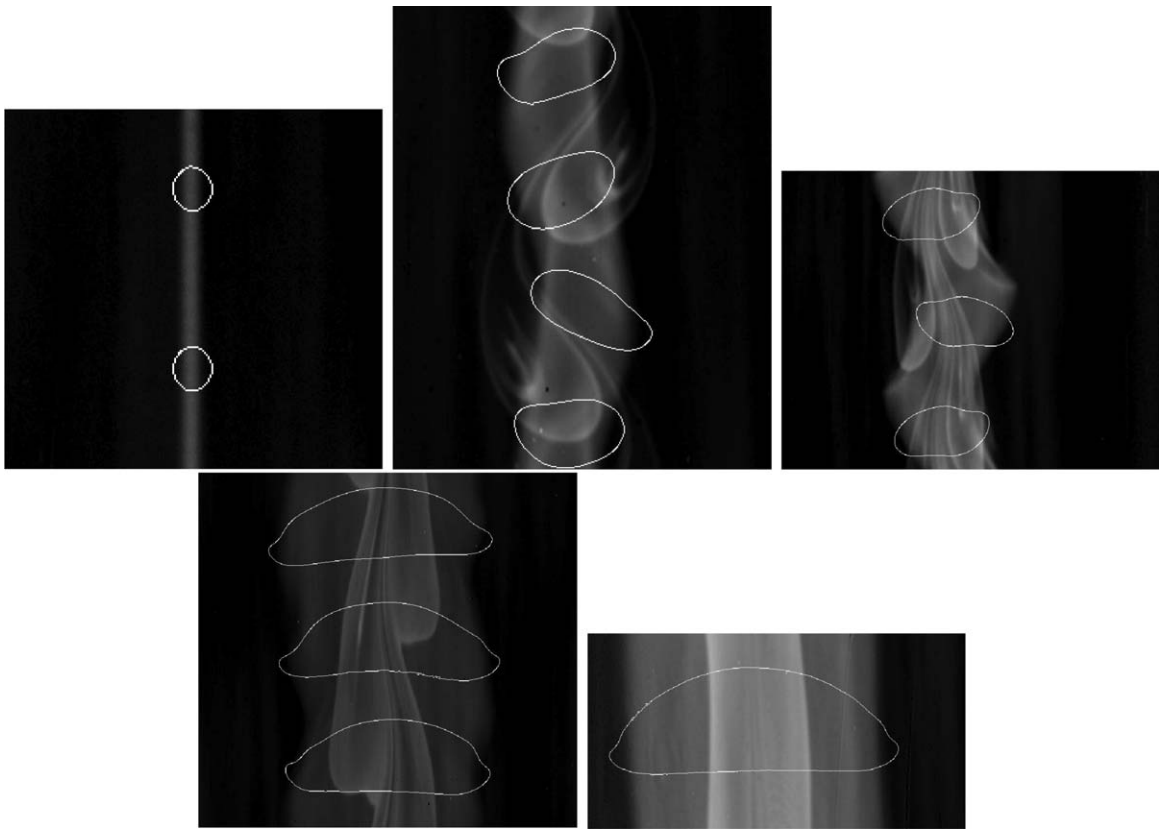

Figure 8. Averaged images in bubble wakes at various Archimedes numbers with superimposed bubble contours.
From left to right, starting from the top: *Ar* = 210; 1,400; 2,380; 6,340; and 11,000.

$R_{fluo}=F/F_0$. Black pixels thus correspond to regions where there is no oxygen whereas lighter pixels correspond to regions of greater oxygen concentration. However, at this stage, grey levels have not been converted into oxygen concentration because, due to the nonlinearity of Stern-Vollmer relation, this will require further assumptions. Figure 7 shows that oxygen deposit is a steady single straight stripe at the lower Archimedes number (Figure 7a), a complex periodic pattern at intermediate *Ar* (Figures 7b–f) and a combination of nearly straight stripes at $Ar=$ 18,000 (Figure 7g). These features are consistent with what is known concerning the bubble dynamics[14] and the evolution of the wake with *Ar*: steady for $Ar \leq$ 100, unsteady and periodic for Archimedes numbers in the range $[100-10,000]$, and steady again for $Ar \geq 10{,}000$.

Whatever the value of *Ar*, the intensity and the extend of the oxygen deposit is related to the bubble diameter, its trajectory and the structure of its wake. Oxygen is transferred to the liquid films and to the peripheral interfacial region so that the deposit in the wake combines both contributions in a nontrivial way. To identify each contribution it is useful to have some information about the dynamics of the films and of the flow going past the periphery of the bubble. The liquid films between the bubble and the walls are expected to exist all along the bubble trajectory and to be at rest because the interface is mobile.[14]

In Figure 8, we have reported some images of the fluorescence in the wake of a bubble for various *Ar* and superposed some bubble contours as it passes within the observation window. For a bubble at $Ar \approx 210$, oxygen is transferred in a thin straight stripe. For the other Archimedes numbers, the contribution of the film to mass transfer is easily identified as an almost homogeneous large stripe deposit which follows the bubble path oscillations and which horizontal extend is slightly lower than that of the bubble. For intermediate values of *Ar*, the deposit in the film is combined with oxygen collected in vortices (8b, c). For the highest *Ar*, the contribution from the films has a greater lateral extension than that from the peripheral interface (8d, e).

Some instantaneous velocity fields in the liquid phase, measured by particle image velocimetry (PIV), are reported in Figure 9 for Archimedes numbers similar to cases b–e of Figure 8. The presence of periodic structures of oxygen captured in vortical regions as in case b of Figure 8 is related to vortex shedding observed for similar Archimedes numbers in Figure 9a. The oxygen transferred from the bubble through the peripheral interface is collected in these vortices that are released at the bubble rear and are rapidely immobilized due to the shear stress at the walls. Figure 9b shows the velocity field near a bubble in an oscillatory regime similar to that of case c in Figure 8. Such bubbles have strong shape oscillations, and vortex shedding has evolved as compared to case $Ar = 1{,}500$. The vortices, still unsteady, are more elongated in the longitudinal direction and are closer to each other. They are trailed by a column of ascending fluid entrained by the bubble. When increasing Archimedes number, the oxygen transferred from the bubble periphery is therefore collected in more and more elongated and closer periodic fluid structures as illustrated in Figures 8c, d. Finally Figure 9c shows that for the biggest bubbles with stationary wake, the oxygen from the peripheral interface is collected in the central part of the wake by the converging flow past the bubble. For the case e in Figure 8, the oxygen located in the central part of the deposit

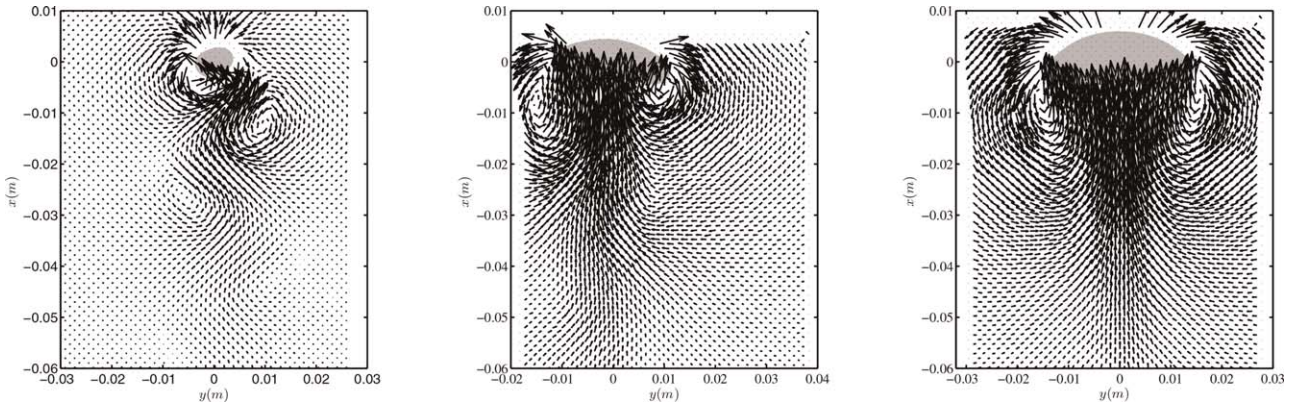

Figure 9. Instantaneous PIV measurements in the wakes of bubbles with various Archimedes numbers.

From left to right: *Ar*= 1,500 (a); 4,750 (b); and 7,050 (c).

comes then in some extend from the free periphery of the bubble.

Coming back to Figure 7 it is important to notice that the periodic structures that accumulate oxygen are clearly superimposed to the deposit from the film without interaction (see for example Figures 7b–d). This states that oxygen originating from the two regions of the interface has been deposited by independent 2D in-plane liquid motions. We can also observe that, except for $Ar=$ 18,000, the oxygen distribution due to the liquid films is not spatially uniform as the film thickness varies during bubble path oscillations. It is still relevant however to consider the oxygen deposit as consisting of a first part issued from the films and expected to be located near the walls, and of a second part issued from the peripheral interface and expected to be distributed in a layer the thickness of which is of the order of magnitude of the gap size.

Coming back to Figure 6 too, it is worth mentioning that a dark halo is visible in bubble front, particularly for the case at $Ar=$ 6,340. The presence of this halo is not a lighting artefact as it does not appear when we inject nitrogen bubbles instead of oxygen bubbles. This dark region is the signature of oxygen transfer to the region upstream of the bubble. It has been observed for bubbles in the range $Ar=$ 1,000–12,000 and its width, δ_n, has been measured and proved to increase between 1 and 4 mm approximately. This order of magnitude, $\delta_n/d \approx 0.2$ for $Ar \geq 1{,}200$, is far greater than the mass boundary layer thickness δ_m that can be estimated for a clean interface: $\delta_m/d \approx Pe^{-1/2}$ where $Pe=V_b d/D$ is the Peclet number. The presence of oxygen in front of the bubble thus results from convective transport toward this region. The fundamental mechanism at the origin of this oxygen accumulation is not still understood. But two phenomena could be involved. First, due to a possible evaporation of ethanol between the front and the rear part of the bubble, a gradient of surfactant could appear leading to a Marangoni effect. This could generate an advective transport from the rear to the front of the bubble along the peripheral interface as described in the study of anomalous wakes closed on themselves by Bush.[33] The second possibility is related to specific vorticity distribution in front of a dipole travelling in a thin layer, the dipole being a representation of the perturbation that a bubble induces in the flow. The confinement may indeed produce a spanwise vortex in front of a dipole,[34] which was observed, nevertheless, quite distant from the front of the dipole in shallow water. It would be interesting to explore the flow near the confined bubble at a sufficient small scale to determine which mechanisms are involved, but this is not under the scope of this study.

Even if it is, at this stage, difficult to quantify the images of fluorescence in terms of concentration, valuable information about the patterns of oxygen deposit, such as their characteristic lengths and displacements, can be deduced from images of Figure 7. An example of such an analysis is presented in Figure 10 for the case of a bubble at $Ar=$ 1,200. The transverse profiles of fluorescence quenching $(1-R_{fluo})$ are picked up along the lines *A–D* in Figure 10a and plotted in Figure 10b. The evolution of fluorescence may thus be observed for nearly half a wave-length of the oxygen pattern. The wave-length of this pattern is identical to that of the bubble motion and can be obtained from the Strouhal measurements given in Roig et al.[14] It is here approximately equal to 6d. The amplitude of the transverse displacement of the borders of the large stripe region (typically 0.5d) is almost equal to the bubble horizontal displacement. The width of the deposit from the films is similar to the bubble diameter. Several points located on lines *A* to *D* are shown in the transverse profiles of 10b. The point denoted α and subsequent circles on the various profiles in Figure 10b belong to the same stripe that has been streched and folded in a vortical structure released by the bubble. We can thus estimate its maximum transverse extension, which is 1.3d. Point β and associated square symbols belong to the same profile along line *B* and to the deposit in the films. The differences between the corresponding fluorescence quenching intensities are the signature of the heterogeneity of the amount of oxygen deposited in the film, which probably results from variations of concentration and from modulations of the thickness of the films during the periodic path of the bubble. Point γ is located on the profile *D* which coincides with the maximum of quenching. The maximum quenching effect averaged over the gap is nevertheless difficult to interpret because the fluorescence in point γ combines fluorescence from deposits into the films and from the periphery where it is transported by unsteady vortices.

Measurement of Mass Fluxes and Discussion

The total mass transfer rate Φ from the bubble is the mass of oxygen *M* deposited in a window of observation divided by the time T_w spent by the bubble to cross this window. For a window of vertical extension L_w, we can estimate $T_w=L_w/V_b$ where V_b is the mean velocity of the bubbles in the vertical

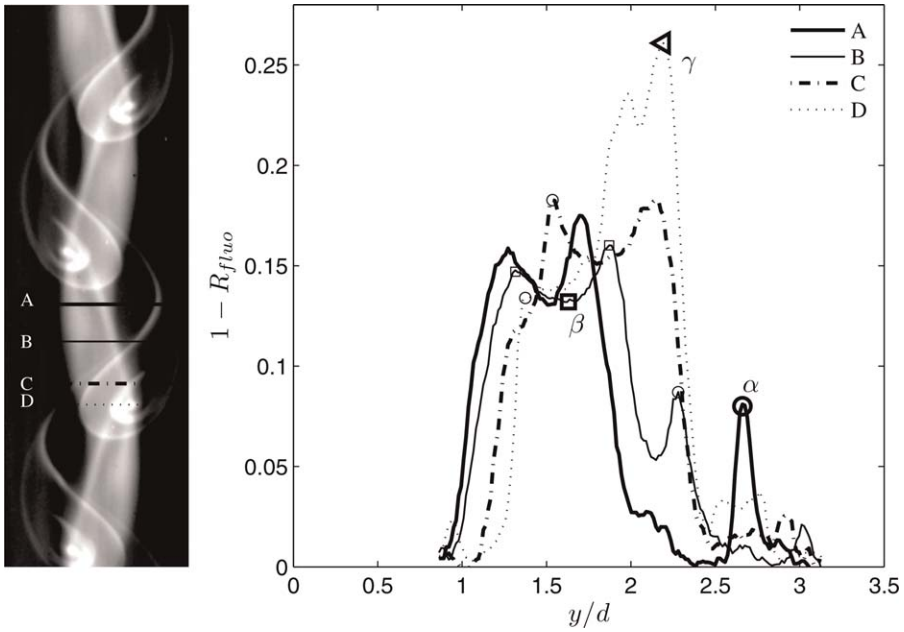

Figure 10. Quenched fluoresced-light intensity distribution at short time after deposit by a bubble at *Ar*=1,200.

The image is an average of 25 images taken every 0.1s, 1.6 s after bubble passage. The various transverse profiles are picked up along lines *A–D*. Points α, *β*, and *γ* are, respectively, attached to regions where oxygen comes from (α) mass transfer at the peripheral surface and has been engulfed in a vortex, (*β*) the liquid films, and (*γ*) both surfaces. The small symbol ○ plotted on each profile indicates the intensity detected at the intersections between the various lines A–D with the thread of oxygen collected by a vortex to which point α belongs. It is associated to various values of fluorescence on a given thread of a vortical structure. For profile *B* all the square symbols □ report intensities belonging to the oxygen deposit in liquid films: their variation indicates that some fluorescence modulations are present in the films.

direction. The mass M is easily calculated if the spatial in-plane distribution $\bar{C}(x,y)$ of the concentration is known and is then given by $M=w\int \bar{C}(x,y)dxdy$.

Due to the nonlinearity of the Stern-Vollmer relation and to the nonuniformity of the oxygen deposit over the gap of the cell, it is difficult to determine $\bar{C}(x,y)$ from fluorescence measurements during the bubble passage or a short time after. However, as described in next section, the mass of gas deposited by a bubble at each given location (x, y) can be determined from the local concentration $\bar{C}(x,y)$ a long time after the bubble passage.

Direct measurement of the total mass transfer rate

To measure the total mass transfer rate, images were recorded at a time T_{diff} after the bubble passage, when all fluid motion has vanished and the initial oxygen heterogeneity across the gap has been homogenized by molecular diffusion. The time T_{diff} is greater than the characteristic diffusion time scale $w^2/(4D)$ which is around 125 s. In this case, the Stern-Vollmer relation (1) can be directly applied to calculate $\bar{C}_\infty(x,y)=\bar{C}(x,y,t\to\infty)$ from the measurements of fluorescence intensity ratio $F(t\to\infty)/F_0$ denoted $R_{fluo\infty}$. Note that for $t<T_{diff}$, molecular diffusion transports oxygen in the plane of the cell. Figure 11 presents two images recorded at time $t>w^2/v\approx 1$s, when all fluid motion has vanished due to viscous dissipation. The first one (on the left) is recorded at $t=$ 1.6 s before molecular diffusion has changed the initial spatial mass concentration distribution. The second image (on the right) is registered at $t=$ 240 s when concentration has become uniform across the gap. This image is blurred due to in-plane diffusion of oxygen. The in-plane transverse profiles of concentration plotted in Figure 11 also show the changes of the fluorescence intensities due to redistribution of oxygen across the gap. For example, we observe that in the region where there is only a deposit from the films (along line C_2) the value of $1-R_{fluo}$ at short time (around 0.12) is lower than that at long time ($1-R_{fluo\infty}\approx 0.17$) which is consistent with the Stern-Vollmer relation and with mass conservation.

The total mass flux ϕ is obtained from

$$\phi=\frac{wV_b}{L_wS_i}\int \bar{C}_\infty(x,y)dxdy, \tag{3}$$

where $S_i=S_p+2S_f$ is the area of the bubble surface. To normalize the mass flux, we introduce a Sherwood number Sh based on the diameter of the bubble d: $Sh=\phi d/(DC_s)$. Figure 12 shows the evolution of the Sherwood number with the Peclet number ($Pe=V_bd/D$). Despite some dispersion of the data, a fit of the experimental results provides a scaling as

$$Sh=1.126\ Pe^{1/2} \tag{4}$$

Data scattering provides an idea of the experimental error that decreases when the bubble size increases. Major uncertainties come from the measurement of the area where oxygen is deposited in the integral evaluation of relation (3) and from that of bubble velocity. Both measurements are less accurate for oscillating bubbles at low Archimedes number because the global area of deposit is more complex due to vortices collecting oxygen and because low frequency PIV imaging is less precise for bubble velocity measurements in the oscillating regime. It is worth noticing that in a complementary test, not reported here, performed with a different mixture, mass transfer measurement was performed for one bubble and proved to be in agreement with the present scaling law. The mixture consisted in water (91% w/w) and ethanol (9% w/w) with a concentration of complex of Ruthenium of 12.5 mg/L different from the one used in this study. This indicates that, for the

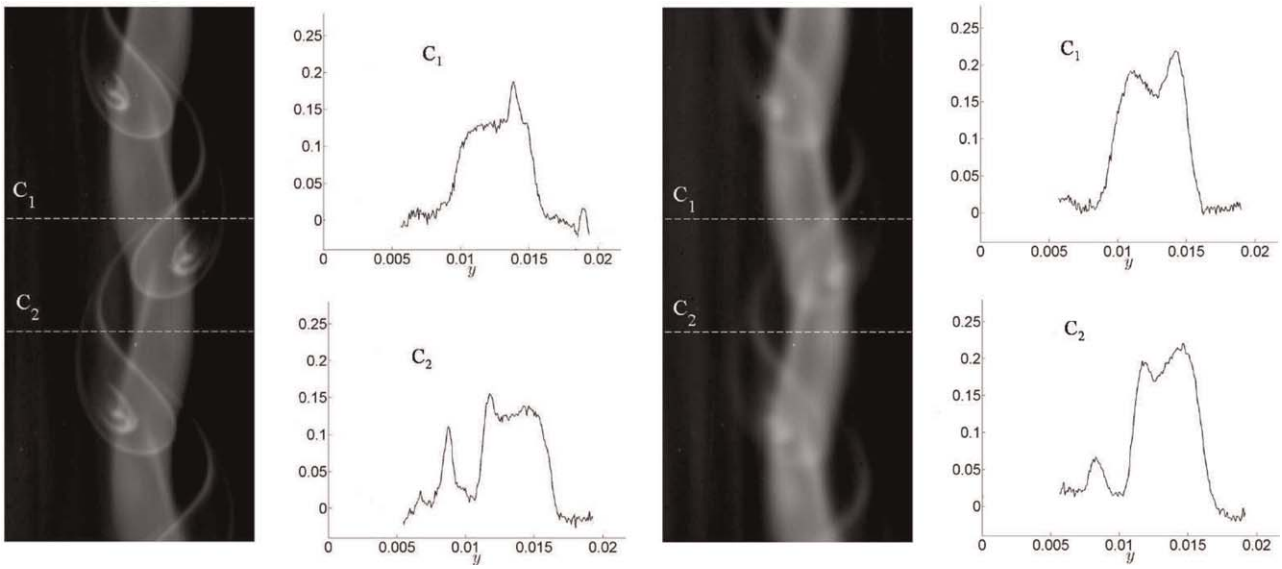

Figure 11. Comparison between intensity distributions ($1-R_{fluo}$) recorded 1.6 s (to the left) and 240 s (to the right) after a bubble passage (Ar = 1,200).

The pictures are obtained by averaging 25 consecutive images taken at 10 Hz. The graphs show profiles along the marked lines C_1 and C_2.

explored range of fluorescent dye concentration, mass transfer is probably unaffected by the presence of this dye.

Estimation of the mass flux from the liquid films

In this section we present a method to measure the contribution to mass transfer rate from the liquid films between the bubble and the walls, using images recorded at short times.

In the wake of a bubble, the deposit of oxygen may be modeled as the combination of three regions: a first one where dissolved oxygen comes from the films only (region F), a second one where all oxygen comes from bubble periphery (region P) and a third one where the oxygen comes from both films and periphery (region FP). Each region has an area in the (x, y) plane denoted by S_F, S_P, and S_{FP}, respectively. Figure 13 shows (for two bubbles of different Ar) the region F in light grey, the region P in dark grey and region FP in black, all detected on an image recorded at short time. These regions have been quantitatively distinguished by the use of grey level thresholds.

The evaluation of the various masses of oxygen related to these areas depends at first on the thresholds used for the measurements of the areas in image analysis. Area S_F can be easily estimated from its borders location. It may be seen, however, that S_P and S_{FP} are not easy to measure for the cases at intermediate Archimedes number ($Ar =$ 1,200 in Figure 13) due to the limited dynamic range of the fluorescent signal and to the sensitivity to thresholding. For small bubbles with vortex shedding (cases a–d in Figure 7), the area of region P is quite small and therefore too sensitive to thresholding to be reported. We thus gave up on calculating a reliable estimation of S_P in these cases. For higher Ar, as in case b in Figure 13, region P does not exist and it is possible to estimate S_{FP} from its external borders. For S_F and S_{FP} the uncertainty induced in the area estimation by the choice of the threshold is small. It has been evaluated to be less than 12% in the worst case.

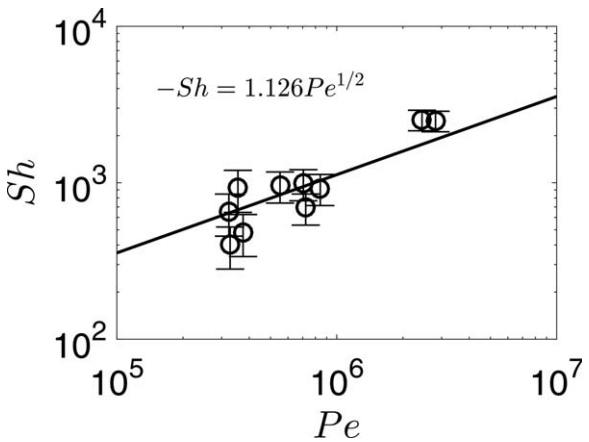

Figure 12. Dimensionless total mass transfer rate.

The Stern-Vollmer relation being nonlinear and oxygen concentration being nonuniform across the gap at short time, it is impossible to make a direct determination of the value of $\bar{C}(x, y)$ in the three regions from fluorescence measurements. But, even if, for any given point (x, y) in an image at short time, the associated local distribution of oxygen concentration along the z-direction (normal to the plates) has not been measured, we can build a model for this distribution. This model of concentration distribution is then related to the measured fluorescence signals using relation (2) to determine the effective mass of oxygen deposited in the gap.

As detailed hereafter, the order of magnitude of the thickness of the mass boundary layer in the liquid film between the bubble and the wall is known. The evolution by diffusion of the concentration layers near the walls after the bubble passage can thus be estimated. At the time of measurement, the mass of oxygen coming from a film is contained within a thin layer of width l_F that can be estimated from the time after the bubble passage. We also know that the peripheral surface of the bubble has an in-gap width of the order w, which leads to a deposit all across the gap. We therefore model the in-gap distribution of concentration $C(z)$ as shown in Figure 14. When a point is in the region F, we consider that oxygen concentration is concentrated in two thin layers close to the walls. For a

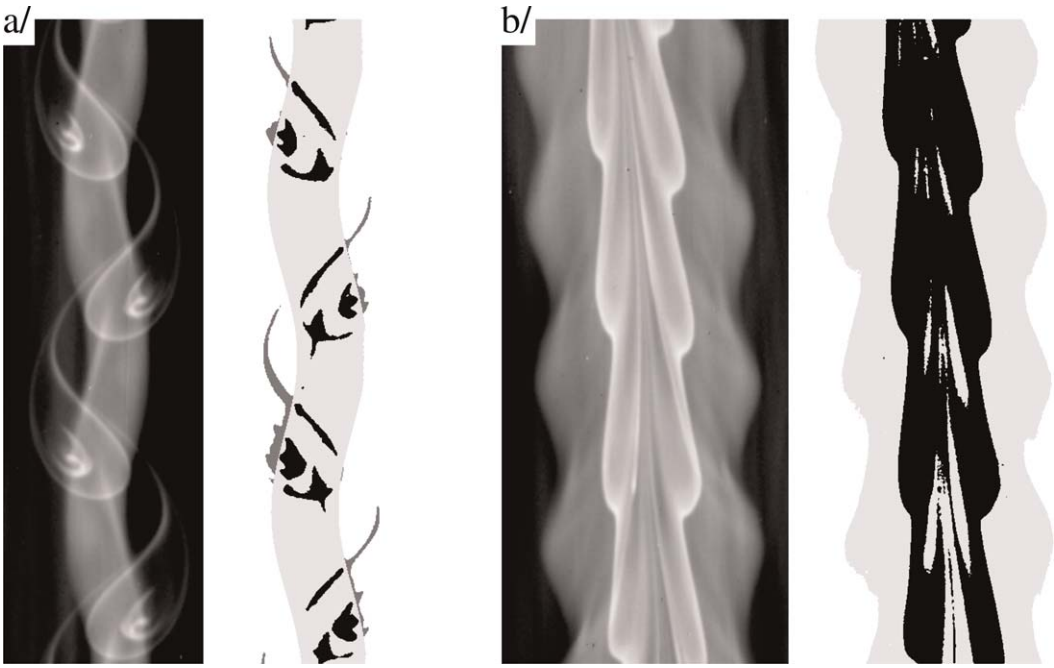

Figure 13. Detection of the three regions of oxygen deposit by grey-level analysis.

(a) Ar = 1,200; (b) Ar = 5,096. For each case the initial image (on the left) and the detected regions (on the right) are provided (light grey: region *F* from films; dark grey: region *P* from periphery; black: region *FP* from both films and periphery).

point in region P, we assume that the concentration is uniformly distributed over the whole gap. This is consistent with the 2D global character of the flow, but remains an approximation since the bubble curvature may influence the mass transfer. In region FP, we consider that the concentration profile is represented by the sum of the previous distributions (Figure 14). As the normalized standard deviation of grey levels over each area (S_F, S_P, or S_{FP}) never exceeds 9%, the in-plane distribution of concentration is modeled as uniform in each region. A unique value of fluorescence characterizes each region and is denoted R_{fluoF}, R_{fluoP}, and R_{fluoFP}, respectively. They are related to the corresponding uniform values of the concentration C_F and C_P to be determined (C_F and C_P are defined in Figure 14). This is, also, an approximation because of the presence of modulations of the deposit in the film region. For the estimation of the total amount of mass transferred in the film region it is nevertheless a rather good model.

Using the assumed distribution of concentration in the gap reported in Figure 14, the following relations between the fluorescent signal R_{fluo} and the characteristics of the model (C_F, C_P, l_F) are obtained from the Stern-Vollmer relation (2) for each region as

$$R_{fluoF}=\frac{2l_F}{w}\frac{1}{1+K_{SV}C_F}+\frac{w-2l_F}{w} \tag{5}$$

$$R_{fluoP}=\frac{1}{1+K_{SV}C_P} \tag{6}$$

$$R_{fluoFP}=\frac{2l_F}{w}\frac{1}{1+K_{SV}C_F}+\frac{w-2l_F}{w}\frac{1}{1+K_{SV}C_P} \tag{7}$$

If the three unknown values of l_F, C_F, and C_P can be determined from these relations and the measured values of fluorescence ratios, the concentration of dissolved oxygen averaged over the gap may then be calculated in each region: $\bar{C}_F=(2l_F/w)C_F$, $\bar{C}_P=C_P$ and $\bar{C}_{FP}=(2l_F/w)C_F+((w-2l_F)/w)C_P$. Then, from the estimations of S_F, S_P, and S_{FP}, one can obtain the mass coming from the film $M_F=\bar{C}_F w(S_F+S_{FP})$ or from the periphery $M_P=\bar{C}_P w(S_P+S_{FP})$. As explained before, in this study, we focus on mass transfer from the films due to uncertainties in S_P estimation.

For cases showing the existence of the three regions, the values of l_F, C_F, and C_P could be calculated from the fluorescence measurements by solving relations (5)–(7) all together. However, the simultaneous identification of parameters of

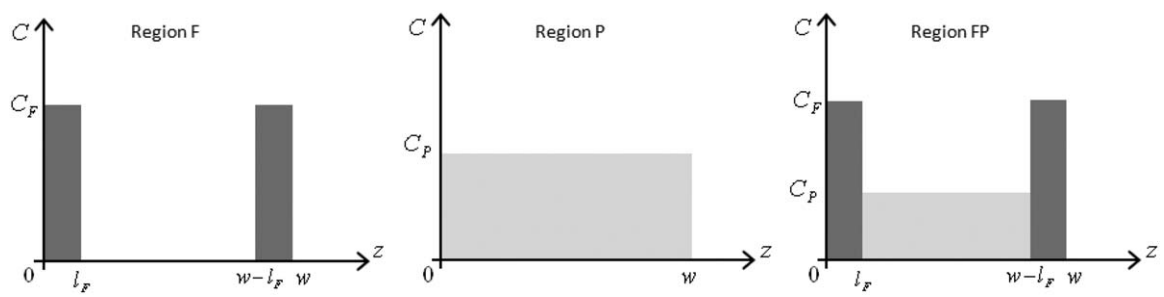

Figure 14. Model of spatial distribution of oxygen across the gap: in region *F* oxygen originates from the films, in region *P* from the bubble periphery and in region *FP* oxygen is transferred from both films and periphery.

different physical nature and different orders of magnitude is sensitive to the experimental uncertainty, and has then been found unreliable. This simultaneous identification was tried for several time-averaged images and gave discrepancies of more than 40% for the values of l_F. In this work, it has been preferred to estimate l_F using a specific method, described in the following. This method also solves the problem of estimating the three parameters from the two relations (5) and (7) when area P does not exist, as it is the case for bubbles e to f of Figure 7. To calculate l_F, the idea is to use the fluorescent signal recorded at long time $R_{fluo\infty}$ and the mass conservation between short and long time. Since $M=w\int \bar{C}_\infty(x,y)dxdy=w\int \bar{C}_{model}(x,y)dxdy$, mass conservation writes

$$\int \frac{w}{K_{SV}}\frac{1-R_{fluo\infty}}{R_{fluo\infty}}dxdy=2l_FS_FC_F+wS_PC_P+S_{FP}(2l_FC_F+wC_P). \tag{8}$$

This relation must be satisfied and can be used to check the validity of the measurements. A mass conservation argument may also be applied to a small zone pertaining to the area where oxygen comes from the films. Neglecting in-plane diffusion, it writes $wC_{F\ \infty}=2l_FC_F$. This leads to

$$2l_F/w=\frac{(1-R_{fluoF})(1-R_{fluoF\ \infty})}{(1-R_{fluoF\ \infty})-R_{fluoF\ \infty}(1-R_{fluoF})}. \tag{9}$$

We have used this relation to determine l_F from measurements of R_{fluoF}. For all the bubbles, the values of l_F are found to be equal to 100.4 μm within an incertainty of $\pm 5.5\mu$m. These values are in agreement with the length expected from diffusive transport of the mass boundary layer in the liquid film that develops between the bubble and a wall. In fact, the film thickness h, the mass boundary thickness δ_m and its growth due to diffusion leading to the deposit width at wall l_F can be evaluated. The non-dimensional film thickness can be estimated as $h/w \approx 1.34Ca^{2/3}/(1+3.35Ca^{2/3})$ from the work of Aussillous and Quéré[35] where $Ca=\mu V_b/\sigma$ is the capillary number. Depending on the slip or no slip condition at the bubble interface, the thickness of the mass boundary layer scales as either $\delta_m/d \approx Pe^{-1/2}$ or $\delta_m/d \approx Pe^{-1/3}(h/d)^{1/3}$. Quantitatively, the two estimations are not significantly different. During the time interval δt (up to 4 s) between the bubble passage and the recording at short time, the mass boundary layer growths by molecular diffusion and the width l_F may be estimated by $l_F \approx \delta_m+\sqrt{D\delta t}$. The values of l_F given by such a model are in the range 96–109 μm for the whole range of Ar. They are in good agreement with the values of l_F deduced from mass conservation and fluorescence measurements given before.

Using relations (5) and (9) with measurements of R_{fluoF} and $R_{fluoF\ \infty}$, the concentration C_F in the deposit from the films can be calculated. It was always of order 3–6 mg/L far lower than the saturation value C_s. For a given bubble, the evaluated total quantity of dissolved oxygen derived from short-time images and from long-time images must also be the same as expressed by relation (8). For all the measurements, the total mass of oxygen evaluated for short-time and long-time images match with less than 13% discrepancy. The coherence in the identified values of l_F, and the agreement with the model for mass deposit thickness, prove the pertinence of the model for dissolved oxygen distribution between the plates, and validates the approach adopted in this work.

Figure 15 reports both the total mass transfer rate and that coming from the films (in g/s) as a function of the diameter.

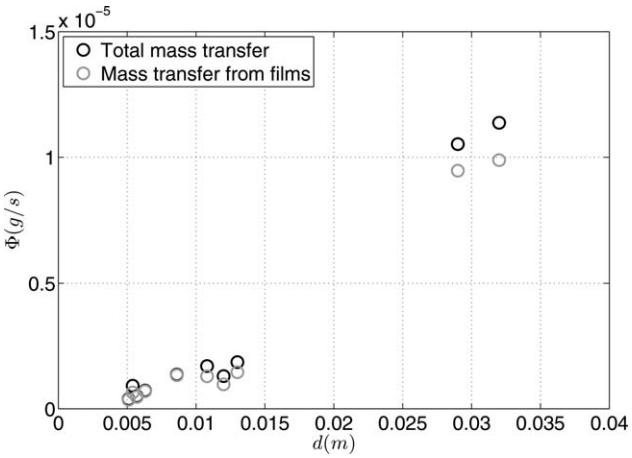

Figure 15. Comparison of the total rate with the rate from the films (g/s).

It shows that the mass transfer rate from the films is the dominant contribution.

The transfer rate from the films (Φ_f), estimated from measurements in region F at short time, is only slightly lower than the total mass rate. This indicates that the mass transfer from the films is dominant. Figure 16 shows the dimensionless rate of transfer in the films $Sh_f=\phi_f d/(DC_s)$ where $\phi_f=\Phi_f/2S_f$ is the mass flux in the films. This Sherwood number is well described by the following relation

$$Sh_f=1.066\ Pe^{1/2}. \tag{10}$$

This scaling is consistent with films where oxygen concentration is below the saturation and with a fully mobile bubble interface described by a slip condition for the liquid. We can therefore retrieve the origin of this scaling from a mass boundary layer analysis: the liquid being at rest in the films, the mass boundary layer width δ_m could be estimated from a simplified advection-diffusion balance that writes $V_bC_S/d \approx DC_S/\delta_m^2$. It would thus scales as $\delta_m/d \approx Pe^{-1/2}$ in complete agreement with relation 10. However, we cannot definitively conclude about the exact structure of the mass boundary layer in the films. In fact, if we assume that a no slip condition applies at the bubble interface, then the scaling comes from a modified balance $(V_b\delta_m/h)C_S/d \approx DC_S/\delta_m^2$ due to the change of

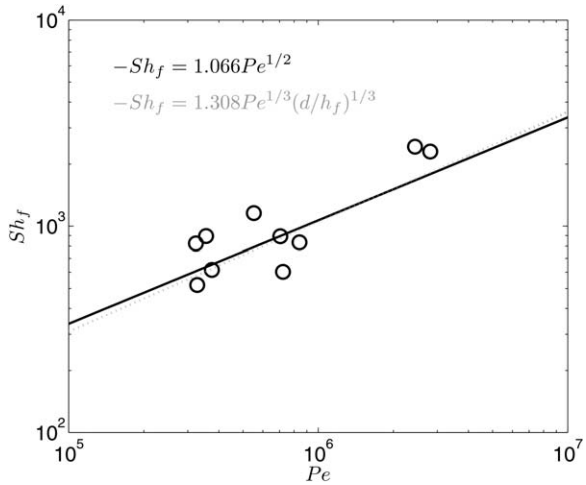

Figure 16. Scaling law for mass transfer in the films between the bubble and the walls.

velocity field in the mass boundary layer and one gets $\delta_m/d \approx (Ped/h)^{-1/3}$. This relation, used with the model of Aussillous and Quéré[35] for the estimation of the film thickness h provides a new scaling law where the Sherwood number is proportional to $(Pe.d/h)^{1/3}$. And a satisfactory fit of the experiments can also be obtained that writes $Sh_f = 1.308(Pe.d/h)^{1/3}$. It is plotted in grey on Figure 16 where it is observed that it is not possible to conclude definitively on the most representative scaling law. There is, however, no direct measurements of the mass transfer in the films, neither any experimental description of the film thickness to conclude definitively on the mass boundary layer in the films. We thus decided to privilegiate the scaling law given in relation (10) that relies only on measured parameters.

Concluding Remarks

An original experimental method, based on laser fluorescence quenching, has been developed to measure oxygen transfer around isolated bubbles rising in a thin gap. The deposit of oxygen in the bubble wake has been characterized for a large range of Archimedes numbers ($200 \leq Ar \leq 18,000$) by the spatial in-plane distribution of fluorescent light emitted by a fluorophore present all across the cell gap. This in-plane distribution revealed that there are two main regions of interfacial oxygen transfer and transport: (1) in the thin liquid films between bubble and walls, oxygen is deposited and then transported by molecular diffusion and (2) in the interfacial region of the bubble swept by the external high-Reynolds number flow, oxygen is released and collected in the wake. This wake is associated to a global in-plane motion of the liquid through the whole gap between the plates. Some visualizations of instantaneous fields of fluorescence around bubbles also show that in front of the bubbles there exists an extended region where oxygen migrates. Such a large region reveals that convection modifies the mass boundary layer and enhances the mass transfer. The mechanism at the origin of this convection has not been identified yet.

Due to the non-linearity of Stern-Vollmer relation between fluorescence and dissolved oxygen concentration and to the non-homogeneous distribution of oxygen through the gap, it is not possible to determine the oxygen concentration averaged across the gap in a straightforward manner from the fluorescence image. To measure the spatial in-plane distribution of oxygen, it has thus been necessary to analyze images taken at long times after bubble passage when oxygen concentration has been homogenized across the gap by molecular diffusion. Total mass transfer rate has therefore been calculated from these measurements at long time. A scaling law has been proposed for the Sherwood number as a function of the Peclet number, based on the equivalent in-plane diameter d of the confined bubble.

Using this scaling law $Sh(Pe)$ (Eq. 4), the total mass rate can be compared to that occuring at the interface of a bubble with the same volume rising freely in an infinite medium. The in-plane diameter d of a confined bubble is to be related to the diameter of a free bubble by relation $d_{eq} = (3/2d^2w)^{1/3}$. For a free bubble, we adopt the scaling law $Sh = 2/\sqrt{\pi}.Pe^{1/2}(1-2.89/\sqrt{Re})$ given by Clift et al.[36] for a sphere with a clean interface. The rise velocity can be calculated by relation $We_c/We + 0.505/Fr = 1$ (from the same Ref. 36) where $We = \rho V_b^2 d_{eq}/\sigma$ is the Weber number based on the surface tension σ, $We_c = 2.3$ a critical Weber number, and $Fr = V_b^2/(gd)$ the Froude number. For a bubble of diameter $d = 5$mm we have a direct measurement of the total mass rate in confined geometry of approximately 4.10^{-7} g/s. Using the scaling law (4) resulting from a fit of all the data it is modified to 5.3 10^{-7} g/s. For the corresponding free bubble of diameter $d_{eq} =$ 3.3mm the total mass rate estimated from the scaling law given by Clift et al. (1978) is about 6.6 10^{-7}g/s. The mass rates are very similar for such small bubbles, but when the bubble diameter increases, the increase of interfacial area in the confined configuration favors a greater total mass rate as compared to unconfined bubble. As an example, for a bubble of diameter $d = 3$cm (corresponding to $d_{eq} = 1.1$cm) the oxygen mass transfer rate is about twice that of a free bubble of same volume (8.8 10^{-6}g/s as compared to 4.1 10^{-6}g/s).

The contribution of the films to mass transfer was estimated from fluorescence images recorded at short time, assuming a simplified concentration profile through the gap. The profile is of piecewise constant shape with various regions of uniform concentration originating from the deposit in the films, from the peripheral interface or from both of them. The dimension of the film deposit in the gap was determined from mass conservation combining fluorescence data measured in this region at short and long times. The concentration in the liquid films was then calculated. The measurements indicate that the liquid films are far from being saturated in oxygen. A scaling law relating the Sherwood number Sh_f characterizing mass transfer in the films is also provided.

Another interesting result of this local analysis of mass transfer at high Schmidt number is that for a given bubble size (or Peclet number), the mass fluxes measured either for the total mass transfer or for the transfer in the films are not so different (Eqs. 4 and 10). The contribution of the liquid films to mass transfer is the major contribution to the mass rate because, having similar mass flux, their surface is the most important for interfacial exchange as compared to the peripheral surface.

Open questions still remain. One concerns the exploration of the flow in front of the bubble that leads to convection of oxygen in the vicinity of the interface. Another concerns the exact nature of the flow in the liquid films. Depending on the presence or absence of contaminants at the bubble interface no-slip or zero-shear-stress boundary condition applies. We have no direct method to conclude. However the present mass transfer scaling law indicates that the interface could be clean of contaminants or that the films are thick enough to minimize the effects of shear stress on mass transfer in the films. Also a direct measurement of the mass rate coming from the interfacial transfer at the peripheral interface and an analysis of the instantaneous concentration distribution in the vicinity of the bubble would be of great interest. Moreover, in a swarm of confined bubbles, mass transfer depends on the bulk concentration of oxygen. The way the results obtained for an isolated confined bubble are modified in a bubble swarm is thus a thrilling question.

As compared to unconfined bubbles in 3D bubble columns, the confinement of bubbles in a planar cell increases the interfacial mass transfer. This intermediary confined bubbly flow could thus be interesting for applications as it provides simultaneously efficient mass transfer and mixing.

References

1. Bercic G. Influence of operating conditions on the observed reaction rate in the single channel monolith reactor. *Catal Today* 2001;69: 147–152.
2. Roberge DM, Ducry L, Bieler N, Cretton P, Zimmermann B. Reactions at Lonza. *Chem Eng Technol*. 2005;28(3):318–323.

3. Haase S, Bauer T, Langsch R, Lange R. (2009) Mass transfer in small channels with slug-flow under reacting conditions. In: *Proceeding of WCCE8*, Montreal, August 2009.
4. Jensen KF. Microreaction engineering—is small better? *Chem Eng Sci.* 2001;56:293–303.
5. Kreutzer MT, Kapteijn F, Moulijn JA. Shouldn't catalysts shape-up? Structured reactors in general and gas-liquid monolith reactors in particular. *Catal Today.* 2006;111:111–118.
6. Irandoust S, Andersson B, Bengtsson E, Siverstrom M. Scaling up a monolithic catalyst reactor with two-phase flow. *Ind Eng Chem Res.* 1989;28:1489–1493.
7. Vandu CO, Liu H, Krishna R. Mass transfer from Taylor bubbles rising in single capillaries. *Chem Eng Sci.* 2005;60:6430–6437.
8. Van Baten JM, Krishna R. CFD simulations of mass transfer from Taylor bubbles rising in circular capillaries. *Chem Eng Sci.* 2004;59: 2535–2545.
9. Irandoust S, Ertle S, Andersson B. Gas-liquid mass transfer in Taylor flow through a capillary. *Can J Chem Engng.* 1992;70:115–119.
10. Bercic G, Pintar A. The role of gas bubbles and liquid slug lengths on mass transport in the Taylor flow through capillaries. *Chem Eng Sci.* 1997;52:3709–3719.
11. Yue J, Chen G, Yuan Q, Luo L, Gonthier Y. Hydrodynamics and mass transfer characteristics in gas liquid flow through a rectangular microchannel. *Chem Eng Sci.* 2007;62:2096–2108.
12. Shao N, Gavriilidis A, Angeli P. Mass transfer during Taylor flow in microchannels with and without chemical reaction. *Chem Eng J.* 2010;160:873–881.
13. Dietrich N, Loubière K, Jimenez M, Hébrard G, Gourdon C. A new direct technique for visualizing and measuring gas-liquid mass transfer around bubbles moving in a straight millimetric square channel. *Chem Eng Sci.* 2013;100:172–182.
14. Roig V, Roudet M, Risso F, Billet AM. Dynamics of a high-Reynolds-number bubble rising within a thin gap. *J Fluid Mech.* 2012;707:444–466.
15. Filella A, Ern P, Roig V. 0scillatory motion and wake of a bubble rising in a thin gap cell. *J Fluid Mech.* 2015;778:60–88.
16. Bouche E, Roig V, Risso F, Billet AM. Homogeneous swarm of high-Reynolds-number bubbles rising within a thin gap. Part 1. Bubble dynamics. *J Fluid Mech.* 2012;704:211–231.
17. Bouche E, Cazin S, Roig V, Risso F. Mixing in a swarm of bubbles rising in a confined cell measured by mean of PLIF with two different dyes. *Exp Fluid.* 2013;54:1552
18. Bouche E, Roig V, Risso F, Billet AM. Homogeneous swarm of high-Reynolds-number bubbles rising within a thin gap. Part 2. Liquid dynamics. *J Fluid Mech.* 2014;758:508–521.
19. Almeras E, Cazin S, Roig V, Risso F, Augier F, Plais C. Time-resolved measurement of concentration fluctuations in a confined bubbly flow by LIF. *Int J Multiphase Flow.* 2016;83:153–161.
20. Dani A, Guiraud P, Cockx A. Local measurement of oxygen transfer around a single bubble by planar laser-induced fluorescence. *Chem Eng Sci.* 2007;62:7245–7252.
21. Vazquez G, Alvarez E, Navaza J. Surface tension of Alcohol+Water from 20 to 50°C. *J Chem Eng Data.* 1995;0:611–614.
22. Pecar D, Dolecek V. Volumetric properties of ethanol-water mixtures under high temperatures and pressures. *Fluid Phase Equil.* 2005;230:36–44.
23. Jimenez M, Dietrich N, Hébrard G. Mass transfer in the wake of non-spherical air bubbles quantified by quenching of fluorescence. *Chem. Eng. Sci.* 2013;100:160–171.
24. Wilke CR, Chang P. Correlation of diffusion coefficients in dilute solutions. *AIChE J.* 1955;1:264–270.
25. Jimenez M, Dietrich N, Cockx A, Hébrard G. Experimental study of O2 diffusion coefficient measurement at a planar gas-liquid interface by planar laser-induced fluorescence with inhibition. *AIChE J.* 2013; 59(1):325–333.
26. Reid RC, Prausnitz JM, Poling BE. *The Properties of Gases and Liquids*, 4th ed. New York: McGraw-Hill Book Company, 1987.
27. Crimaldi JP. Planar laser induced fluorescence in aqueous flows. *Exp Fluid.* 2008;44:851–863.
28. Moghaddas JS, Trägårdh C, Kovacs T, Östergren K. A new method for measuring concentration of a fluorescent tracer in bubbly gas-liquid flows. *Exp Fluid.* 2002;32:728–729.
29. Roy S, Duke SR. Visualization of oxygen concentration fields and measurement of concentration gradients at bubble surfaces in surfactant-contaminated water. *Exp Fluid.* 2004;36:654–662.
30. Stohr M, Schanze J, Kovacs T, Khalili A. Visualization of gas-liquid mass transfer and wake structure of rising bubbles using pH-sensitive PLIF. *Exp Fluid.* 2009;47:135–143.
31. François J, Dietrich N, Guiraud P, Cockx A. Direct measurement of mass transfer around a single bubble by micro–PLIFI. *Chem Eng Sci.* 2011;66:3328–3338.
32. Herlina JGH. Application of LIF to investigate gas transfer near the air-water interface in a grid-stirred tank. *Exp Fluid.* 2004;37:341–349.
33. Bush JWM. The anomalous wake accompanying bubbles rising in a thin gap: a mechanically forced Marangoni flow. *J Fluid Mech.* 1997;352:283–303.
34. Albagnac J, Lacaze L, Brancher P, Eiff O. On the existence and evolution of a spanwise vortex in laminar shallow water dipoles. *Phys Fluid.* 2011;23:086601. doi:10.1063/1.3611419.
35. Aussillous P, Quéré D. Quick deposition of a fluid on the wall of a tube. *Phys Fluid.* 2000;12(10):2367–2371.
36. Lochiel A, Calderbank P. Mass transfer in the continuous phase around axisymetric bodies of revolution. *Chem Eng Sci.* 1964;19: 471–484.